

Numerically Simulating Seawall Overtopping

Derek Causon¹, David Ingram¹, Clive Mingham¹,
Jun Zang¹, Keming Hu² and Jian Guo Zhou¹

Abstract

Developments in computational modelling of storm waves propagating in the coastal surf zone and overtopping at sea walls and related structures is reported. The AMA-ZON suite of 1D and 2D Plan shallow water models are used for the calculations. The models employ a modern Riemann-based upwind scheme in a finite volume form for use on boundary-conforming meshes. Sea wall structures are approximately represented using a steep bed slope. Breaking waves are modelled as steep moving fronts represented by bore waves. Comparisons with measured data show good agreement for sloping sea walls. Results are presented for the effects of wave obliquity on overtopping discharges including cases involving Mach stem formation. For vertical and recurved sea walls, an accurate model of wave breaking is required.

1 Introduction

Storm waves breaking in the coastal surf zone and crashing over a sea wall are a violent natural phenomenon. Structural failure of the sea defence may be linked strongly to peak rather than mean discharges. Levels of risk impact also differ significantly depending on the wave characteristics, including wave obliquity, and on the geometry of the structure. Recent studies [1] have also shown increased extreme wave heights in the early stages of depth-limited breaking when nonlinear shoaling is of importance. No safe guidance is yet available to link the severity of peak overtopping flows and velocities to particular wave or structure characteristics.

The total volume of sea water overtopping in a particular storm is generally well predicted by current methods [2, 3, 4]. However, recent work [5] has demonstrated that current formulae significantly underestimate peak overtopping discharge under shallow water conditions when wave impacts occur at the structure. Studies by Allsop

¹Centre for Mathematical Modelling and Flow Analysis, Manchester Metropolitan University, Chester Street, Manchester M1 5GD, United Kingdom

²MMU and Posford Duvivier, Bretton Centre, Peterborough PE3 8DW, United Kingdom

et al [6] under PROVERBS have shown that this effect is particularly severe for steep or vertical walls with beaches or rock mounds and its effects have not previously been included in prediction methods. Analysis by Besley et al [7] shows that methods that exclude these effects can severely underestimate overtopping under breaking wave conditions.

Both the shallow water equations and the Boussinesq equations contain nonlinear convective terms where problems tend to arise numerically. Classical centrally-differenced schemes become unstable in areas where the flow becomes transcritical, or where flow discontinuities occur.

Non-hydrodynamic prediction methods have limitations on the shape of beach, sea wall profiles and wave conditions. Such methods may be applicable only to simple sea wall profiles such as a single slope with one berm breakwater. Kobayashi et al [8] showed that the long wave equations could be applied successfully to describe wave motion at an onshore coastal structure. Similar methods have been reported by van Gent [9], Zou and Dodd [10] and Watson et al [11]. These methods ignore the detailed structure of the breaking wave and model the dynamics of a wave attack on a structure with steep fronts represented by bores. The long wave equations include the shallow water equations and the Boussinesq equations with dispersive terms to make the equations valid in deeper water. The work of Watson et al [11] suggests that the Boussinesq equations work reasonably well for non-breaking waves in the foreshore area, and methods based on the shallow water equations were good in the swash zone.

Following developments in aeronautical CFD, schemes based on modern upwind methods have been applied to the shallow water and Boussinesq equations. Such schemes resolve bore waves and hydraulic jumps accurately without numerical oscillations. Recent studies have shown encouraging results for transcritical flow, wave mechanics, run-up and overtopping [12, 13, 14]. A 2-D Plan shallow water model, part of the Manchester Metropolitan University (MMU) AMAZON suite of computer models [15, 16], employs a modern Riemann-based upwind finite volume scheme of this type on a patched or Cartesian cut cell (CCC) boundary-fitted mesh. Breaking waves are simulated by a travelling bore wave.

2 Governing Equations

2.1 The Shallow Water Equations

The shallow water equations (SWE) are a reduced form of the depth averaged Navier-Stokes equations which represent the conservation of mass and momentum. Admissible solutions may admit flow discontinuities such as bore waves.

In differential conservative form the equations are

$$\frac{\partial \mathbf{U}}{\partial t} + \frac{\partial \mathbf{F}}{\partial x} + \frac{\partial \mathbf{G}}{\partial y} = \mathbf{Q}_s + \frac{\partial \mathbf{F}_v}{\partial x} + \frac{\partial \mathbf{G}_v}{\partial y} \quad (1)$$

where

$$\mathbf{U} = \begin{bmatrix} \phi \\ \phi u \\ \phi v \end{bmatrix}, \mathbf{F} = \begin{bmatrix} \phi u \\ \phi u^2 + \frac{\phi^2}{2} \\ \phi uv \end{bmatrix}, \mathbf{G} = \begin{bmatrix} \phi v \\ \phi uv \\ \phi v^2 + \frac{\phi^2}{2} \end{bmatrix}$$

$$\mathbf{Q}_s = \mathbf{A} + \mathbf{B} + \mathbf{C} + \mathbf{D}$$

$$\mathbf{A} = \begin{bmatrix} 0 \\ fv\phi \\ -fu\phi \end{bmatrix}, \mathbf{B} = \begin{bmatrix} 0 \\ \frac{g}{\rho}\tau_{xw} \\ \frac{g}{\rho}\tau_{yw} \end{bmatrix}, \mathbf{C} = \begin{bmatrix} 0 \\ -\frac{g}{\rho}\tau_{bx} \\ -\frac{g}{\rho}\tau_{by} \end{bmatrix}, \mathbf{D} = \begin{bmatrix} 0 \\ \phi gb_x \\ \phi gb_y \end{bmatrix},$$

\mathbf{F} and \mathbf{G} are the convective flux vectors, \mathbf{A} is the Coriolis force term, \mathbf{B} is the wind shear stress term, \mathbf{C} is the bed shear stress term, \mathbf{D} is the bed slope term and the viscous stress flux vectors \mathbf{F}_v and \mathbf{G}_v are

$$\mathbf{F}_v = \begin{bmatrix} 0 \\ \sigma_{xx}\frac{\phi}{\rho} \\ \tau_{yx}\frac{\phi}{\rho} \end{bmatrix}, \mathbf{G}_v = \begin{bmatrix} 0 \\ \tau_{xy}\frac{\phi}{\rho} \\ \sigma_{yy}\frac{\phi}{\rho} \end{bmatrix}.$$

In the above, f is the coriolis force, g is the acceleration due to gravity, ρ is the water density, u, v are the velocities in the x and y directions respectively, ϕ is the geopotential ($= gh$, h is the water depth), τ_{xw}, τ_{yw} are the wind shear stresses and τ_{bx}, τ_{by} the bed shear stresses in the x, y directions, $\sigma_{xx}, \sigma_{yy}, \tau_{xy}, \tau_{yx}$ are the normal and shear stress terms respectively and b_x, b_y are the bed slopes (measured downwards) in the x, y directions.

The integral form of the equations is

$$\frac{\partial}{\partial t} \int_A \mathbf{U} dA + \oint_S \mathbf{H} \cdot \mathbf{n} dS = \int_A \mathbf{Q}_s dA + \oint_S \mathbf{H}_v \cdot \mathbf{n} dS \quad (2)$$

where $\mathbf{H} = \langle \mathbf{F}, \mathbf{G} \rangle$, $\mathbf{H}_v = \langle \mathbf{F}_v, \mathbf{G}_v \rangle$ and A is the area enclosed by the control surface S .

The homogeneous part of (2) are the convective flow equations that describe the time evolution of the height and velocity of the water over the physical region of interest in the absence of source terms. These equations are of hyperbolic type and admit discontinuous solutions (e.g. bore waves) In the present work the viscous stress flux vectors \mathbf{F}_v and \mathbf{G}_v and the Coriolis and wind shear stress terms \mathbf{A} and \mathbf{B} are ignored.

The bed friction stresses, τ_{bx} and τ_{by} , may be described using the Colebrook-White equations:

$$\tau_{bx} = \rho C_f u \sqrt{u^2 + v^2}, \tau_{by} = \rho C_f v \sqrt{u^2 + v^2} \quad (3)$$

where $C_f = \frac{1}{8} f_d$ and f_d the Darcy friction factor is given by

$$\frac{1}{\sqrt{f_d}} = -2 \log \left(\frac{k_s}{3.7h} + \frac{2.51}{Re \sqrt{f_d}} \right), \quad (4)$$

where k_s is the roughness height, Re is the Reynolds number and h is the water depth.

3 Numerical Flow Solver

To solve (2), we apply the MUSCL-Hancock finite volume scheme. This is a two-step, high resolution, upwind scheme of the Godunov type. The following description of the scheme relates to the inviscid part of the equation set. The predictor step uses a non-conservative approach that defines an intermediate cell-centre value over a time interval $\Delta t/2$,

$$(A\mathbf{U})_{ij}^{n+\frac{1}{2}} = (A\mathbf{U})_{ij}^n - \frac{\Delta t}{2} \sum_{k=1}^m \mathbf{H}(\mathbf{U}_k) \cdot \mathbf{S}_k^n \quad (5)$$

where A is the cell area, cell side vector \mathbf{S}_k^n is the length of side k multiplied by the outward-pointing unit normal vector \mathbf{n} and m is the maximum number of cell sides. The flux vector function $\mathbf{H}(\mathbf{U}_k)$ is evaluated at each cell side k following a linear reconstruction of the flow solution within each cell, via,

$$\mathbf{U}_k = \mathbf{U}_{ij}^n + \mathbf{r}_k \cdot \nabla \mathbf{U}_{ij}^n \quad (6)$$

where \mathbf{r}_k is the normal distance vector from the cell centroid to side k and $\nabla \mathbf{U}_{ij}^n$ is a limited gradient vector in space (for details of the gradient vector see [13]).

The corrector step is fully conservative. The intermediate solution from the predictor step is used to define a set of left- and right-hand states for a series of Riemann problems. The solution of these Riemann problems provides a set of upwind cell interface fluxes which are used to update the flow solution over the time interval Δt , that is,

$$(A\mathbf{U})_{ij}^{n+1} = (A\mathbf{U})_{ij}^n - \Delta t \sum_{k=1}^m \mathbf{H}(\mathbf{U}_k^L, \mathbf{U}_k^R) \cdot \mathbf{S}_k^n \quad (7)$$

where the upwind flux $\mathbf{H}(\mathbf{U}_k^L, \mathbf{U}_k^R)$ is obtained by solving a local Riemann problem normal to cell interface k and the left- and right-hand states at the interface are calculated by

$$\mathbf{U}_k^L = \mathbf{U}_{ij}^{n+\frac{1}{2}} + \mathbf{r}_k^L \cdot \nabla \mathbf{U}_{ij}^n, \quad \mathbf{U}_k^R = \mathbf{U}_{lm}^{n+\frac{1}{2}} + \mathbf{r}_k^R \cdot \nabla \mathbf{U}_{lm}^n \quad (8)$$

where l and m refer to the right neighbouring cell of cell i, j .

To solve the Riemann problem, the approximate Riemann solver of Harten, Lax and van Leer (HLL) [17] is used.

In the general two dimensional case, the upwind flux for use in (7) is

$$\mathbf{H}(\mathbf{U}_k^L, \mathbf{U}_k^R) \cdot \hat{\mathbf{S}}_k^n = \frac{s_R \mathbf{H}_L \cdot \hat{\mathbf{S}}_k^n - s_L \mathbf{H}_R \cdot \hat{\mathbf{S}}_k^n + s_L s_R (\mathbf{U}_R - \mathbf{U}_L)}{s_R - s_L} \quad (9)$$

where $\mathbf{H}_{L,R} = \mathbf{H}(\mathbf{U}_k^{L,R})$, $\hat{\mathbf{S}}_k^n$ is the outward pointing unit normal side vector to cell side k and suitable wave speed estimates s_L, s_R are given by

$$s_L = \min(\mathbf{q}_L \cdot \hat{\mathbf{S}}_k^n - \sqrt{\phi_L}, u_s - \sqrt{\phi_s}), \quad s_R = \max(\mathbf{q}_R \cdot \hat{\mathbf{S}}_k^n + \sqrt{\phi_R}, u_s + \sqrt{\phi_s}) \quad (10)$$

where

$$u_s = \frac{1}{2}(\mathbf{q}_L + \mathbf{q}_R) \cdot \hat{\mathbf{S}}_k^n + \sqrt{\phi_L} - \sqrt{\phi_R} \quad \text{and} \quad \sqrt{\phi_s} = \frac{\sqrt{\phi_L} + \sqrt{\phi_R}}{2} - \frac{(\mathbf{q}_L - \mathbf{q}_R) \cdot \hat{\mathbf{S}}_k^n}{4}.$$

For shallow water problems with a dry bed, the wave speed estimates (10) are replaced by either (11) or (12) as appropriate [18].

right dry bed:

$$s_L = \mathbf{q}_L \cdot \hat{\mathbf{S}}_{i+\frac{1}{2}} - \sqrt{\phi_L}, \quad s_R = \mathbf{q}_L \cdot \hat{\mathbf{S}}_{i+\frac{1}{2}} + 2\sqrt{\phi_L} \quad (11)$$

left dry bed:

$$s_L = \mathbf{q}_R \cdot \hat{\mathbf{S}}_{i+\frac{1}{2}} - 2\sqrt{\phi_R}, \quad s_R = \mathbf{q}_R \cdot \hat{\mathbf{S}}_{i+\frac{1}{2}} + \sqrt{\phi_R}. \quad (12)$$

The time step employed is:

$$\Delta t = \nu \min(\Delta t_x, \Delta t_y) \quad (13)$$

where

$$\Delta t_x = \min_i \frac{A_{ij}}{|\mathbf{q}_{ij} \cdot \mathbf{S}_{i+\frac{1}{2}j}| + \sqrt{\phi_{ij}} |\mathbf{S}_{i+\frac{1}{2}j}|} \quad (14)$$

with an analogous definition for Δt_y . The Courant number ν was taken in our calculations to be 0.5 which is close to the stability bound based on a linear von Neumann analysis.

Further details of the finite volume method and Riemann solver can be found in [13, 15].

4 Results

4.1 Shallow Water Model AMAZON-1D

Numerical experiments are presented in this section to illustrate the use of AMAZON-1D as a predictive tool in one dimension. The tests include wave overtopping at sloping and vertical sea walls. A sample of results is presented here. Further details, including boundary condition treatments, and more validation test cases can be found in [16]. In the following cases, the coastal structure is represented in the shallow water code using the bed slope terms. Wave overtopping at a wall is therefore simulated in the 1D calculations by means of a steep bed slope. The calculations have been performed on uniform meshes except where otherwise indicated. In the 2D cases, the calculations have been performed on a uniform Cartesian mesh with the cut cell facility to provide a boundary-conforming mesh. This allows a vertical wall to be represented exactly, but a sloping wall is handled via the bed slope terms, as in the 1D case.

4.1.1 wave overtopping at sloping seawalls

Experiments based on regular waves overtopping a sloping seawall with slopes of 1:3 and 1:15 have been reported recently. This data has been used previously by numerical modellers for validation purposes [19]. The sea wall profiles are illustrated in Fig. 1, where d_t , d_s and R_c represent water depth below SWL at the seaward boundary,

water depth below SWL at the toe of the seawall and the crest level above SWL. The parameters for 20 runs are presented in Table 1 for a “deep sea” wave height of $H_0 = 1m$. The deep sea wave height was transformed to the seaward boundary (H_t) by the use of linear shoaling theory [5]. In this study, sinusoidal waves were used. Bed friction was modelled using the formula:

$$\tau_b = \frac{1}{2}\rho f|u|u_0 \quad (15)$$

where f was set to 0.05. At the right hand boundary, a transmissive boundary condition was used. The landward boundary was set a certain distance behind the crest. The location was different to that used in [19] where the landward boundary was positioned at the moving waterline, or the crest when overtopping occurred. A non-reflective boundary condition was used at the left hand inlet boundary. A uniform mesh with 400 cells was used in all calculations.

The results are presented in Table 1 and Fig. 1. The dimensionless discharge Q^* was defined as

$$Q^* = \frac{Q}{H_0} \sqrt{gH_0} \quad (16)$$

where H_0 is the deep sea wave height and Q^* is the dimensionless average overtopping discharge. For consistency with other workers [19], an average value of Q^* was calculated during the 4th and 5th wave.

The results obtained with the AMAZON model compared well with the measured data. However, AMAZON-1D is numerically more robust and less dissipative than other models [19] using classical difference schemes and a moving boundary treatment for flooding and drying.

Table 1: Comparison of computed results of Q^* using AMAZON, a, with laboratory tests by Saville, b, and numerical model study by Kobayashi and Wurjanto [19], c. $H_o = 1.0m$

| d_t (m) | d_s (m) | R_c (m) | H_t (m) | T (s) | $Q^* \times 10^{-3}$ | | |
|--------------|--------------|--------------|--------------|------------|----------------------|----|----|
| | | | | | a | b | c |
| 3.0 | 0.75 | 0.50 | 0.95 | 4.73 | 39 | 66 | 27 |
| 3.0 | 0.75 | 1.00 | 0.95 | 4.73 | 15 | 41 | 3 |
| 3.0 | 1.50 | 0.50 | 0.95 | 4.73 | 81 | 64 | 53 |
| 3.0 | 1.50 | 1.00 | 0.95 | 4.73 | 24 | 36 | 14 |
| 4.0 | 2.00 | 0.67 | 0.99 | 6.55 | 86 | 90 | 81 |
| 4.0 | 0.75 | 0.50 | 1.08 | 7.98 | 64 | 60 | 54 |
| 4.0 | 0.75 | 1.50 | 1.08 | 7.98 | 11 | 4 | 2 |
| 4.0 | 1.50 | 0.50 | 1.08 | 7.98 | 101 | 94 | 91 |
| 4.0 | 1.50 | 1.00 | 1.08 | 7.98 | 53 | 40 | 45 |
| 4.0 | 1.50 | 1.50 | 1.08 | 7.98 | 24 | 8 | 16 |

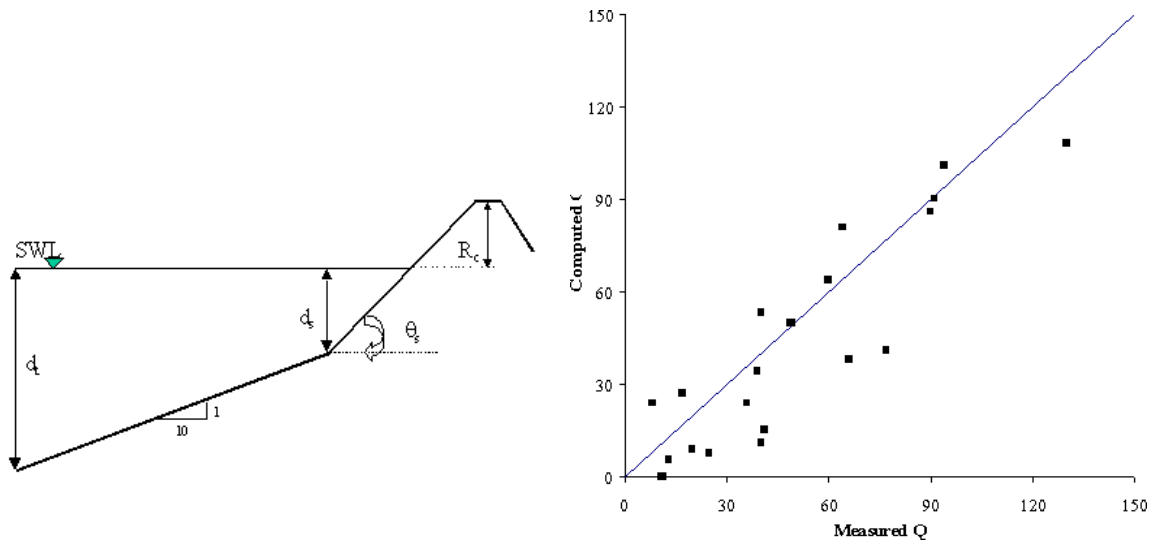


Figure 1: Wave overtopping at a sloping sea wall: Physical arrangement (left) Comparison of computed and measured overtopping discharges, $H_0 = 1.0\text{m}$ (right)

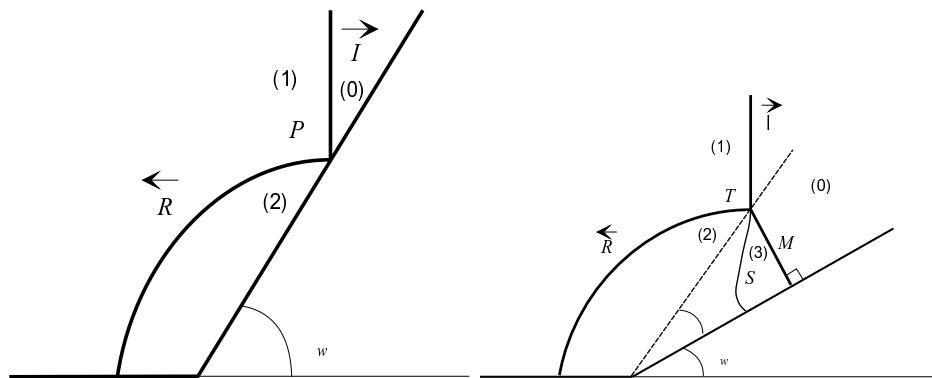


Figure 2: Bore reflection problem: Flow Physics, regular reflection (left) and single Mach reflection (right)

4.2 Shallow Water Model AMAZON-CC 2D (Plan)

Practical considerations require an improved understanding of the effects of wave obliquity on overtopping discharge rates. Real sea wall geometries may exhibit unexpected levels of damage due to complicated wave reflection, focusing and diffraction phenomena caused by the obliquity of the impacting wave and/or its interaction with other waves. For this reason, the observed overtopping discharge at points along the length of a sea wall may depend upon wall obliquity in a complicated manner.

In the case of bore waves, it is known that several types of wave reflection occur at an inclined side wall [13]. The types are regular reflection (RR), single Mach reflection (SMR), transitional (or complex) Mach reflection (TMR) and double Mach reflection (DMR), see Fig. 2. Transition from one type to another depends on the bore Froude number and inclination angle of the side wall into the direction of flow. In the case of RR, the foot of the incident bore wave I (Point P) travels along the

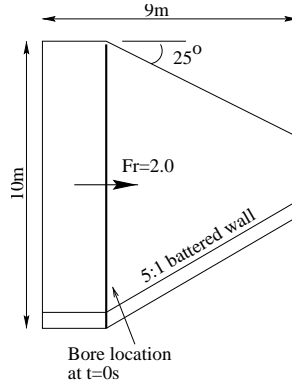


Figure 3: Wave basin: Physical arrangement (single Mach reflection case)

side wall. A reflected wave R travels upstream. Thus, there is a discontinuous jump in water level at points along the side wall lying within the interaction region behind the oblique moving bore. A change in side wall angle and/or bore Froude number induces transition to SMR characterised by a triple point where the incident bore, reflected bore and Mach stem coincide (Fig. 2). This change occurs when acoustic disturbances originating at the deflection point catch up with the reflection point P. This happens when $F_2^P = 1$, where F_2^P is the flow Froude number in state (2) behind the reflected bore with respect to the reflection point P. In the RR case, $F_2^P > 1$.

In the SMR case, the triple point is located off the wall and travels along a straight line ray originating from the point where the side wall deflects. Since the Mach stem is a normal shock, the regions (2) and (3) are separated by a weak slipstream which curves toward the side wall. The rise in water level through the Mach stem is also greater than in other cases of wave reflection. Thus, overtopping at the side wall is more likely to occur in cases involving a regular reflection or Mach stem formation. It is not known whether such wave reflection types occur in the more general case of random waves. It is also not known whether similar reflection patterns occur in the case of oblique bore interaction with a sloping wall. We shall study the latter case first.

The relevant features can be seen in the following examples. In each case a rectangular wave basin has been arranged with an identical deflection angle at the upper and lower walls (Fig. 3) However, while the upper wall is vertical the lower one has a 5:1 slope along its entire length. This case will serve to illustrate in one figure both oblique bore reflection at a vertical wall and the type of interaction that occurs at a similar but sloping sea wall with a concave kink in it. A right travelling bore wave moves along the basin and interacts with each side wall downstream of the deflection point. The problem is completely specified by the bore Froude number F_s and the state in the undisturbed region to the right of the bore. In all cases, $h_R = 1.0\text{m}$ and $u_R = v_R = 0\text{ms}^{-1}$. The state to the left of the bore can be determined from the shock jump conditions [13]

$$\frac{h_L}{h_R} = \frac{\sqrt{1 + 8F_s^2} - 1}{2}, \quad u_L = F_s \left(1 - \frac{h_R}{h_L}\right) c_R \quad (17)$$

where $c_R = \sqrt{gh_R}$ is the local celerity in the undisturbed region ahead of the bore.

A boundary fitted cut cell grid with 120 cells in the flow direction and 320 cells in the transverse direction was used over a $6\text{m} \times 16\text{m}$ region for the RR case. In the SMR case, a grid having 120 cells in the flow direction and 108 cells in the transverse direction was used over a region $10\text{m} \times 9\text{m}$. Fig. 3 illustrates the grid topology for the SMR case. The use of cut cells provides a boundary-fitted capability within a Cartesian mesh. A description of the principles of the cut cell method can be found in [20, 15]. No bed friction terms were included in the computations. The results are shown at a time of $t = 0.8\text{s}$ which is sufficient to illustrate the flow physics whilst halting the calculation before a bore-on-bore interaction occurs between the reflecting bores at the upper and lower walls. Time $t = 0$ corresponds to the arrival of the incident bore at the corner point on the wall. The freeboard at each side wall was set sufficiently high to avoid overtopping. All quoted water heights are referenced to the basin floor as datum. At a bore Froude number of 2 and side wall deflection angle of 60° , a regular reflection (RR) occurs (Fig. 4). The incident and reflected bores meet at a point on the wall (P). The wave structure shown in Fig 2 is clearly visible at the upper (vertical) wall. Through the oblique bore, the water height increases from 1m to 4.5m at the side wall. The line contour figures show a vertical contour in the vicinity of the deflection point on the side wall. This weak feature is left over from the start-up of the calculations and should be ignored. A perspective view of the water surface in the vicinity of the deflection point in the upper wall is shown in Fig. 5. It is noted that the water depth within the interaction region bounded by the incident and reflected bores is higher than that outside in the post incident bore region (where the water height is 2.4m). At the lower wall, the reflection pattern is similar. A weaker reflected bore is found as a result of the wall slope. Within the interaction region, the water height reaches 5.2m behind the foot of the moving bore as the water runs up the sloping side wall. This exceeds the value found at the corresponding point on the vertical wall. The wave structure can be seen in Fig. 5 which shows a perspective view of water surface at the lower wall.

Upon changing the wall deflection angle to 25° at the same bore Froude number, the bore reflection pattern changes from regular (RR) to single Mach reflection (SMR). Again the results are shown at a time of $t = 0.8\text{s}$ and the side wall freeboard is set sufficiently high to avoid overtopping. At the upper wall, a well established triple point is visible with the formation of a Mach stem oriented normal to the vertical wall. The water height rises from 1m to 3m immediately behind the normal shock at the side wall. The side wall freeboard must exceed this value to avoid overtopping. The reflection pattern can be seen in the perspective view of water surface shown in Fig. 7. The slipstream, originating at the triple point and curling toward the side wall, is clearly visible in this figure. The water height inside the interaction region bounded by the incident bore, reflected bore and Mach stem, is significantly higher than that outside. Again, the reflection pattern is similar at the lower wall (Fig. 7). The reflected wave is weaker. Due to the effects of wall slope, the foot of the Mach stem appears to be oriented slightly further forward on the wall. Calculations with a 10:1 slope (not shown) confirm that the foot of the Mach stem moves forward with increasing slope. The water depth at the side wall behind the Mach stem is

3.8m. In the case where the water height exceeds the side wall freeboard, it may be expected that the Mach stem will soon disappear as water is displaced laterally during overtopping.

Calculations were then performed with the height of the sloping wall reduced to 3m above datum. In this case overtopping occurs. Figs. 8 and 8 show perspective views of water surface near the deflection point on the lower wall for the two types of wave reflection. The results are again shown at the time $t = 0.8s$ and illustrate the extent of overtopping along the sloping side wall with the largest lateral encroachment occurring as expected close to the foot of the moving bore. The figures show what appears to be a flat section of water preceding the actual front of the overtopping body of water. This is a numerical effect due to the settings in the flooding and drying algorithm and should be ignored. The Mach stem structure does indeed largely disappear as the water is displaced over the side wall (Fig. 8). The lateral excursion of the overtopping body of water appears higher in the SMR case than the RR case.

The calculations have shown that overtopping discharge may depend nonlinearly on wave obliquity due to regular reflection and Mach stem formation at the wall. The cut cell code predictions with AMAZON-CC can provide a measure of the discharge at points along the sea wall during an overtopping event. Calculations with the incident bore replaced by a solitary wave (not reported) have shown a similar dependence of overtopping discharge on wave obliquity. Further work is underway to establish whether similar trends are observed in the case of random waves.

5 Conclusions

Some developments in computational modelling of storm waves overtopping at sea walls have been reported. These calculations have been carried out with the MMU AMAZON suite of nonlinear shallow water (NLSW) computer models. A one dimensional model AMAZON-1D has been applied to various cases including wave runup at a sloping beach and wave overtopping at sloping and near-to-vertical sea walls. The coastal structure was simulated by means of the bed slope terms and breaking waves modelled as steep wave fronts represented by bores. A modern Riemann-based upwind finite volume scheme was used to integrate the flow equations. Good agreement with data was obtained for wave overtopping at sloping walls. A 2D Plan model AMAZON-CC based on a boundary-fitted cartesian cut cell mesh and bed slope representation of sea wall geometries has been applied to study the effects of wave obliquity on overtopping discharge. With a bore wave model of the incident steep wave front, this was found to depend nonlinearly on the obliquity due to Mach stem formation at the wall. It is not yet known whether similar effects are found with random waves. Further work will address this issue and will extend the modelling to recurved sea wall geometries and wave breaking using a new 2D vertical volume-of-fluid (VoF) model on a Cartesian cut cell mesh.

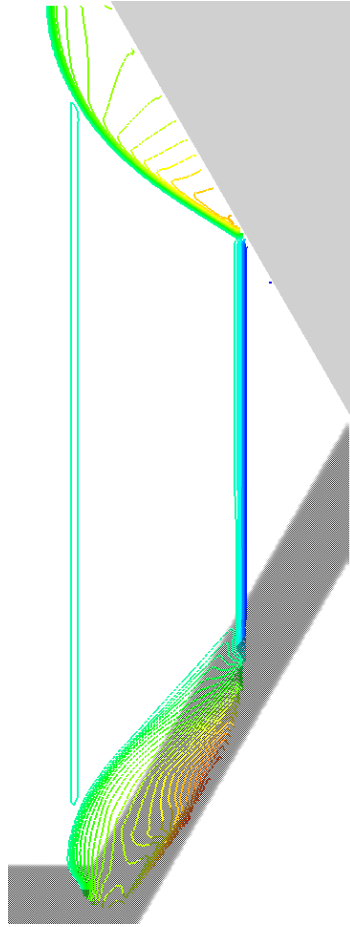


Figure 4: Regular reflection at a sloping wall: Line contours of water height above datum (runup)

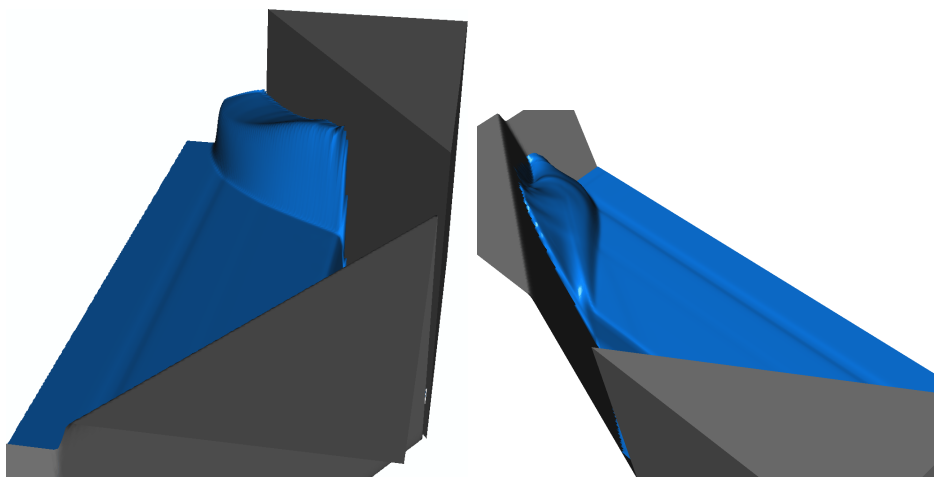


Figure 5: Regular reflection at a sloping wall: Water surface looking towards the upper (vertical) wall (left), Water surface looking towards the lower (sloping) wall (right).

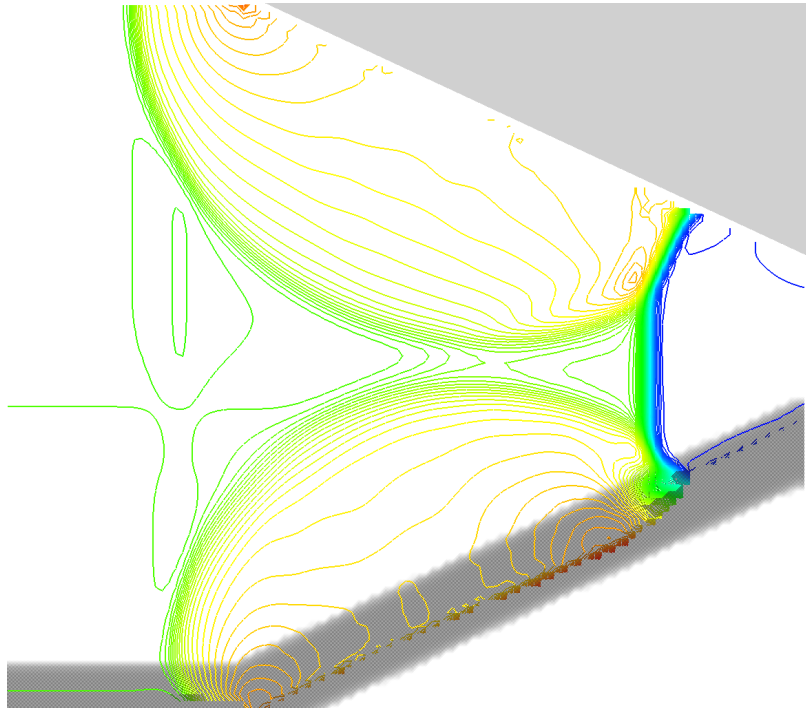


Figure 6: Single Mach reflection at a sloping wall: Line contours of water height above datum (runup)

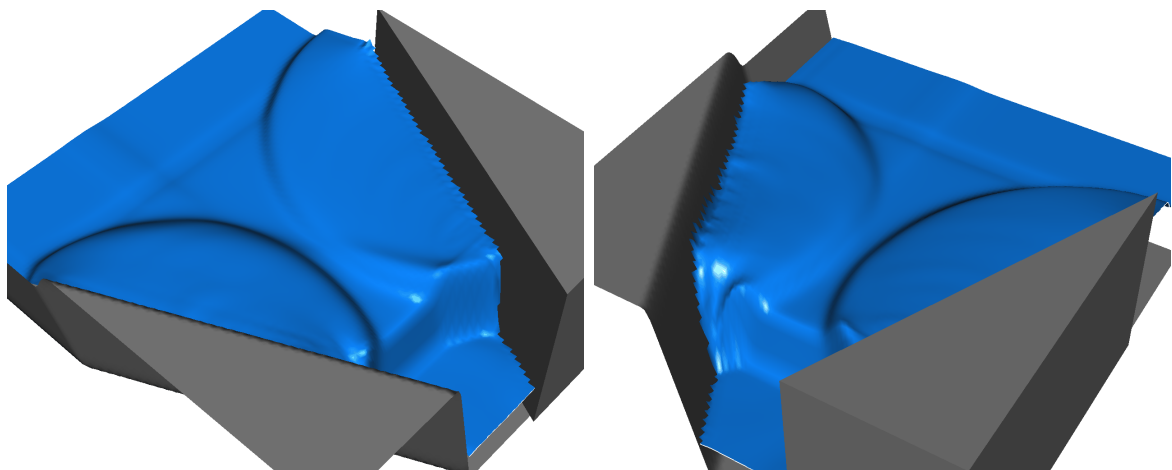


Figure 7: Single Mach reflection at a sloping wall: Water surface looking towards the upper (vertical) wall (left) Water surface looking towards the lower (sloping) wall (right).

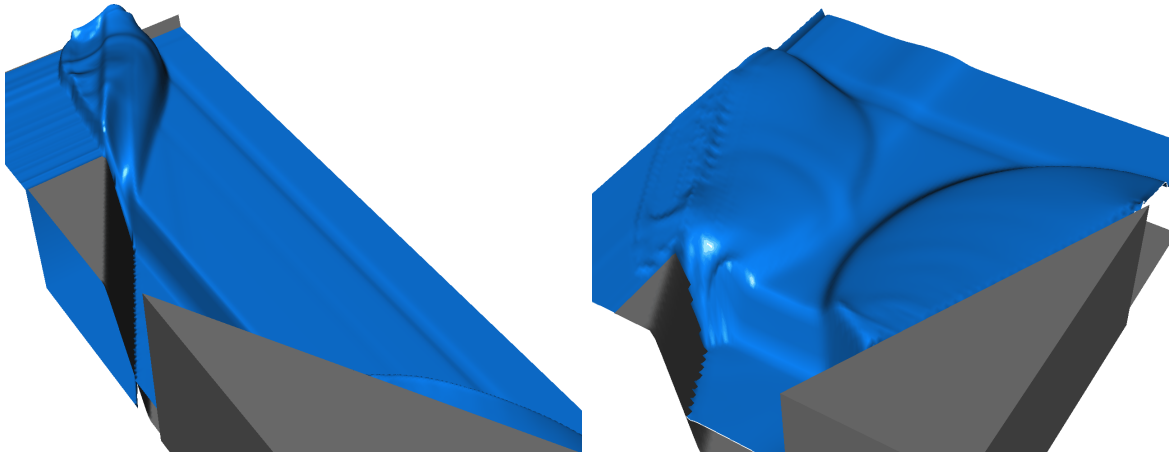


Figure 8: Regular reflection at a sloping wall: Water surface looking towards the lower (sloping) wall, with overtopping (left), Water surface looking towards the lower (sloping) wall, with overtopping (right).

6 Acknowledgements

The authors would like to acknowledge financial support for this project from the UK Engineering and Physical Sciences Research Council (EPSRC) through a research grant (GR M/42428), and Posford Duvivier Ltd for providing data. The authors also wish to express their gratitude to colleagues in the VOWS project (<http://www.vows.ac.uk>) for useful discussions, support and encouragement.

References

- [1] N Durrand and NWH Allsop. Effects of steep bed slopes on depth-limited wave breaking. In *Proceedings of Waves97*. ASCE, 1997.
- [2] MW Owen. Design of seawalls allowing for wave overtopping. Technical Report EX-924, HR-Wallingford, 1984.
- [3] JP De Wall, P Tonjes, and JW van der Meer. Overtopping of sea defences. In *Proceedings of the 25th International Conference on Coastal Engineering*, volume 2, pages 2216–2229, 1997.
- [4] TS Hedges and MT Reis. Random wave overtopping of simple sea walls: a new regression model. *Proceedings ICE: Water, Maritime and Energy*, 130, 1998.
- [5] Y Goda. *Random seas and maritime structures*. Univeristy of Tokyo Press, 1985.
- [6] NWH Allsop, JE McKenna, D Vicinanza, and TTJ Whittaker. New design methods for wave impact loadings on vertical breakwaters and seawalls. In *Proceedings of the 25th International Conference on Coastal Engineering*. ASCE, 1996.

- [7] P Besley, T Stewart, and NWH Allsop. Overtopping of vertical structures: new prediction methods to account for shallow water conditions. In *Proceedings of the Conference on coastlines, structures and breakwaters*. ICE, 1998.
- [8] N Kobayashi and KD Watson. Wave reflection and runup on smooth slopes. In *Proceedings: Coastal Hydrodynamics*, pages 548–563. ASCE, 1987.
- [9] MRA van Gent. The modelling of wave action on and in coastal structures. *Coastal Engineering*, 22:311–339, 1994.
- [10] Z Zou and N Dodd. A nonlinear surf beat model. In *Proceedings of the 24th International Conference on Coastal Engineering*. ASCE, 1994.
- [11] G Watson, TCD Barnes, and DH Peregrine. Numerical modelling of solitary wave propagation and breaking on a beach and runup on a vertical wall. In H Yeh, P Liu, and J Synalakis, editors, *Long Wave Runup*. World Scientific, 1996.
- [12] N Dodd. Numerical model of wave runup, overtopping and regeneration. *Journal of Waterway, Port, Coastal and Ocean Engineering*, 124(2):73–81, 1998.
- [13] CG Mingham and DM Causon. A High Resolution Finite Volume Method for Shallow Water Flows. *Journal of Hydraulic Engineering*, 124(6):605–614, 1998.
- [14] K Hu, CG Mingham, and DM Causon. A bore-capturing finite volume method for open channel flows. *International Journal for Numerical Methods in Fluids*, 28:1241–1261, 1998.
- [15] DM Causon, DM Ingram, CG Mingham, G Yang, and RV Pearson. Calculation of shallow water flows using a cartesian cut cell approach. *Advances in Water Resources*, 23:545–562, 2000.
- [16] K Hu, CG Mingham, and DM Causon. Numerical simulation of wave overtopping of coastal structures using the nonlinear shallow water equations. *Coastal Engineering*, in press.
- [17] A. Harten. On a Class of High Resolution Total Variation Stable Finite Difference Schemes. *SIAM Journal Numerical Anal*, 21(1):1–23, 1984.
- [18] L Fraccarollo and EF Toro. Experimental and Numerical Assessment of the Shallow Water Model for Two Dimensional Dam-break Type Problems. *Journal of Hydraulic Research*, 33(6):843–864, 1995.
- [19] N Kobayashi and A Wurjanto. Wave overtopping on coastal structures. *Journal of Waterway, Port, Coastal and Ocean Engineering, ASCE*, 115:235–251, 1989.
- [20] G. Yang, D. M. Causon, D. M. Ingram, R. Saunders, and P. Batten. A Cartesian Cut Cell Method for Compressible Flows - Part A : Static Body Problems. *Aeronautical Journal*, 101(1001):47–56, 1997.